

Integration of wing-mounted over-wing engines on a mid-range aircraft

Patrick Wegener¹ and Fabian Lange²
German Aerospace Center (DLR), Braunschweig, Germany

Ultra-High Bypass Ratio (UHBR) engines are an important technology for improving the efficiency of future aircraft. However, their large diameter poses a major challenge for their use in conventional under-wing mounted engine configurations due to limited space. A configuration with engines mounted above the wing is not subject to these limitations and therefore offers the potential for improvements in overall aircraft efficiency and performance. Another advantage of this configuration is the acoustic shielding effect of the fan noise toward the ground by the wing. Configurations with this type of engine layout were investigated as part of the German LuFo V project AVACON (AdVanced Aircraft CONcepts). This paper describes the investigated variant of engine integration via a vertical pylon between nacelle lower side and main spar of the wing. To investigate the complex aerodynamic interactions between the engine and the wing, RANS CFD simulations were performed using the DLR code TAU. By optimizing twist and upper surface shape, the wing geometry was adapted to the flow conditions resulting from the engine integration to reduce detrimental aerodynamic installation effects. In general, the influence of the geometric shape of the wing and engine as well as their relative geometric position on the overall drag is more pronounced in such a configuration than in a under-wing engine design. The use of advanced optimization methods is therefore crucial for a successful design.

I. Nomenclature

AVACON	= Advanced Aviation Concepts
CAD	= Computer-aided design
CFD	= Computational fluid dynamics
C_L	= Lift Coefficient
C_D	= Drag Coefficient
DoE	= Design of experiments
MA	= Mach Number
MAC	= Mean aerodynamic chord
UHBR	= Ultra High Bypass ratio
WB	= Wing/Body Configuration
WBE	= Wing/Body/Engine Configuration
WBEP	= Wing/Body/Engine/Pylon Configuration
WBEP T	= Wing/Body/Engine/Pylon Configuration, Twist optimized
WBEP TS	= Wing/Body/Engine/Pylon Configuration, Twist and Shape optimized

II. Introduction

The development of new aircraft is driven by two factors: a reduction in noise and an increase in efficiency. On the engine side, the latter can be increased by means of a higher bypass ratio, which is simultaneously accompanied by an increase in the engine diameter. For this reason, there are limits to this approach in a classic configuration of an under-wing engine arrangement, such as the necessary landing gear length or a detrimental impact on the leading edge high-lift system. An over-wing configuration would not be limited in this respect, and would have the potential to achieve advantages in terms of noise emissions through the shielding effect of the

¹ Research Scientist, DLR, Institute of Aerodynamics and Flow Technology, Lilienthalplatz 7, 38108 Braunschweig

² Research Scientist, DLR, Institute of Aerodynamics and Flow Technology, Virtual Product House @ EcoMaT | Cornelius-Edzard-Straße 15, 28199 Bremen

wing. Due to the interference of the engine with the local supersonic regions on the upper side of the wing, complex flow situations arise, which is why the implementation of these concepts in practice has so far only been carried out in isolated cases.

While such a configuration had already been developed as a commercial aircraft in the 1960s with the intention of being able to take off from poorly paved airfields in the form of the VFW614 [1], this configuration only came into scientific focus at the turn of the millennium due to the noise advantages.

In the study by Brodersen et al. [2], it was shown that an engine position in front of the leading edge of the wing is associated with major aerodynamic challenges. Hooker et al [3] investigated a wider variation of configurations where a trailing edge mounting position showed better aerodynamic performance. For a business jet application, Fujino [4] demonstrated that an advantageous configuration could be developed and converted into a marketable product.

The nationally funded AVACON project addresses these aspects and develops a holistic evaluation of such a configuration. In previous work, preliminary design methods were used to develop a reference configuration with a classic engine configuration for "middle of the market" requirements (Wöhler et al. [5]). The design range is 4,600 nm and a capacity of 257 passengers. For this configuration, a wing with high fidelity CFD was developed as a wing body (WB) configuration for the given cruise conditions (Lange [6]). Within the AVACON project, different concepts for engine integration were investigated:

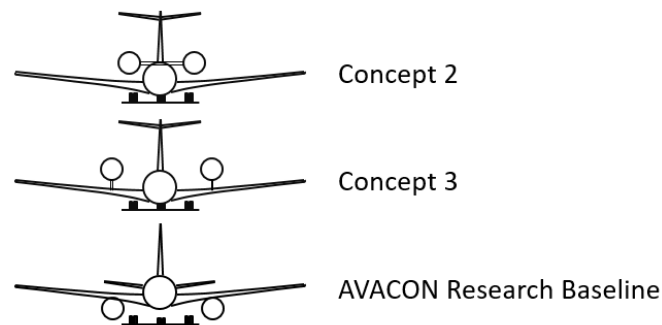


Figure 1 AVACON engine mounting concepts

In Concept 2, the engines are mounted on a pylon in the form of a stub wing on the top of the fuselage. This allows undisturbed flow in the region between the underside of the engine and the wing. While this concept is mechanically complex to implement, Concept 3 takes the approach of attaching the engines to the wing structure. To evaluate the two concepts, the AVACON Research Baseline provides the reference in the form of a classic configuration. For consistency of use within the AVACON project, the nomenclature is not continuous at this point. In all cases, a UHBR engine with a bypass ratio of 16.3 is used, with geometry provided by a consortium partner [7]. While a previous paper by the author [8] described the Concept 2 configuration in detail, the present paper focuses on the Concept 3 configuration.

III. Methodology

Figure 2 shows the sequence of the high-resolution CFD simulations within the project. These are divided into a process chain, which can be run manually or fully automated, and an optimization part for iterative improvement of the design.

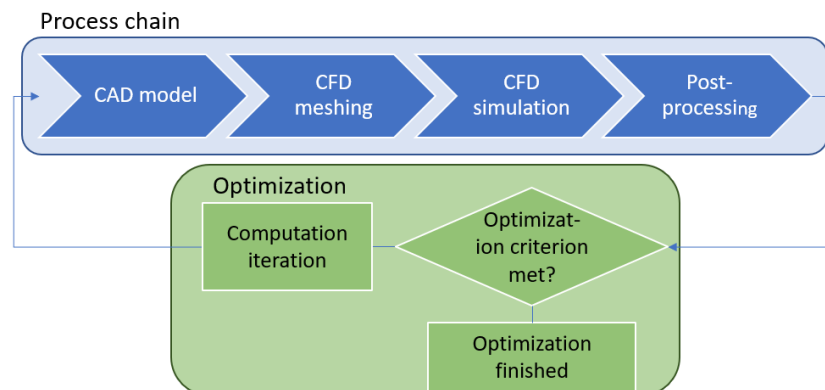


Figure 2 AVACON Process chain

A. Process chain

The process chain begins with the CAD model, which as a parametric CATIA V5 [9] model forms the geometric basis for the subsequent phases. The next step is the generation of the unstructured CFD mesh with the software Centaur from CentaurSoft. In order to represent the expected spectrum of different geometries - especially the pylon modeling – the mesh is generated anew at each iteration. Identical input parameters and CAD based refinement sources ensure comparability - a procedure that has already been applied to different aircraft configurations [5] [9] [10]. An impression of the grid is shown in Fig. 3. The mesh density evolved during the simulation phases between 30 (WB) and 65 (WBEPTS) million nodes.

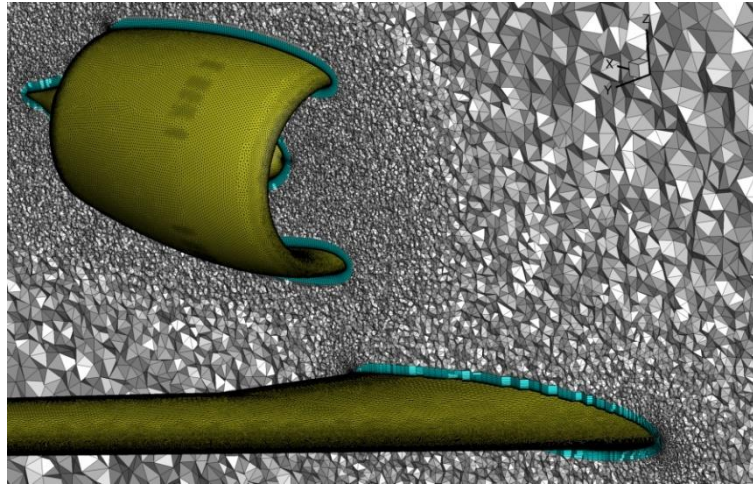


Figure 3 CFD mesh at the engine section

For the cruise flight, 3 stages of different lift coefficients and flight levels are intended. The longest of these stages was defined as a constant boundary condition for the aerodynamic simulations. The lift coefficient C_L is 0.5, the Mach number 0.83 at a flight altitude of 37,000ft. The angle of attack is readjusted during each simulation to achieve the target lift coefficient.

The engines are modeled by the engine boundary condition, assuming the following pressure and temperature ratios:

	Pressure ratio p_v/p_0	Temperature ratio t_v/t_0
Fan	2.022	1.08
Core	1.7020	2.43

Table 1 Engine boundary conditions

The numerical simulations were performed using the DLR TAU code [9]. The turbulence was considered via the Spalart-Allmaras [10], model. In post-processing, the drag components of the entire aircraft as well as the individual components are determined using the area-based drag evaluation tool AeroForce [11], in which force components within the engine stream tube (thrust) are considered separately from force components acting on the external geometry (drag) in order to investigate the overall drag in combination with a thrust-drag bookkeeping.

For a more detailed analysis of the occurring correlations, the drag is further subdivided into components. Figure 4 shows their assignment:

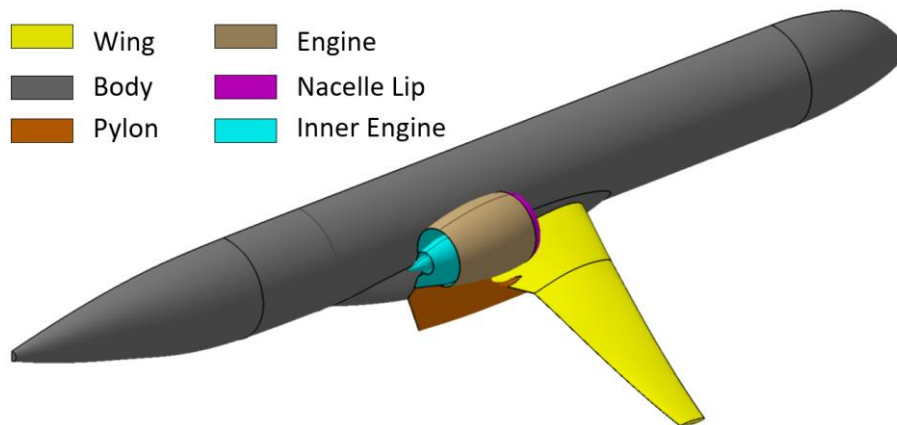


Figure 4 Component boundaries for drag computation

In the following, the abbreviations of the components are used as nomenclature: Wing (W), fuselage/body (B) and pylon (P). The abbreviation "E" refers to the outer contour of the engine. The inner engine is always part of the engine stream tube, while the inlet lip is split at the engine stagnation line: the outer part is accounted for the outer surfaces, while the inner part belongs to the engine stream tube. The components treated in the considered configuration are coded by the abbreviations: consequently, the configuration shown in Figure 4 represents the WBEP configuration.

B. Optimization

For optimization, the process chain is run through fully automatically, always with the aim of minimizing the total drag. For this purpose, DLR's own "Powerful Optimization Tool" (POT) [14] is used, which is based on a surrogate model-based approach. The process can be divided into three phases:

- 1) Design of Experiments (DoE)
- 2) Surrogate model calculation
- 3) Optimization

First, a design of experiments is performed to cover the parameter space by a defined number of samples. From their results, a surrogate model is formed using the Kriging method [15]. Subsequently, the optimization is started from the surrogate model, which is refined in parallel based on the optimization iterations.

C. Simulation strategy

Within the scope of the project, a sequential optimization approach was intentionally chosen in order to be able to assign the observed aerodynamic effects to the origin, induced by geometric variations. Figure 5 shows the breakdown of the work:

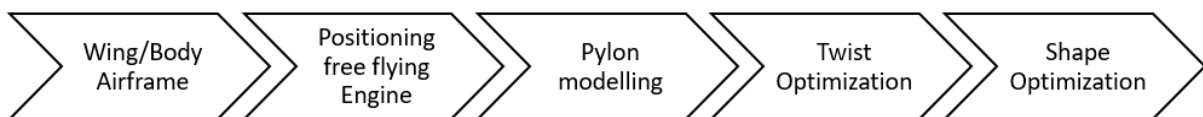


Figure 5 Phases of the simulation strategy

Based on the wing-body (WB) configuration created in previous work within the AVACON context [5], the first phase identifies the spatially dependent interference effects between the engine and the wing by positioning the engine nacelle unconnected to the airframe above the trailing edge of the wing (WBE). As a result of this investigation, a position for the subsequently modeled pylon is determined (WBEP). This configuration is then used to optimize the wing geometry to match the aerodynamics of the wing to the effects caused by the engine. This is done in a two-step approach: in the first step, the wing twist distribution is optimized with fixed wing airfoils, followed by optimization of the wing airfoils using the previously optimized twist distribution. The nomenclature used for these phases is 'WBEPT' for twist- and 'WBEPTS' for shape optimization.

IV. Implementation

A. Engine positioning

The input parameters in the first optimization are the spatial x,y and z coordinates in a parameter space above the trailing edge of the wing, with respect to the mean aerodynamic chord (MAC) length of 5.277m:

Parameter	Lower value	Upper value
x	-0.2	0.2
y	0.85	1.5
z	0.1	0.4

Table 2 Parameter space for the engine positioning

The foremost point of the lower nacelle section through the inlet lip was selected as the reference point for translation (Figure 6). The objective of the optimization was to determine the optimum engine position and to form surrogate models of the drag components of the wing, fuselage and engine.

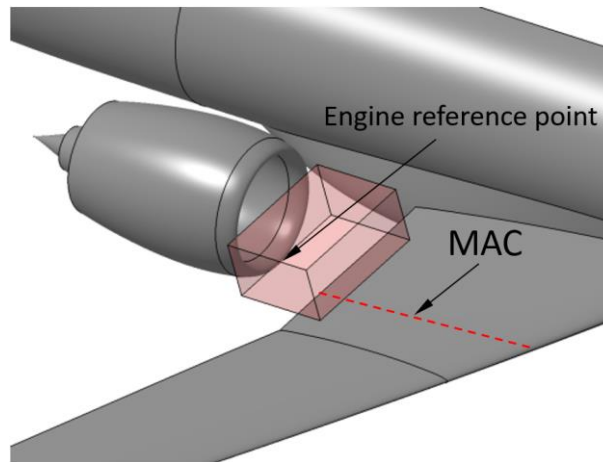


Figure 6 Engine positioning parameter space

For the DoE, 30 iterations were performed, and subsequently a total of 55 iterations for the optimization of the total drag. Compared to the WB configuration, an effect is confirmed here which has already been described in the literature [2] [7]: Due to the impounding effect of the engine nacelle, the flow over the wing in front of it is retarded, which reduces the lift in this area. To satisfy the boundary condition of constant $C_L=0.5$, the angle of attack is increased by about 1° . This results in more lift being generated by the outer wing.

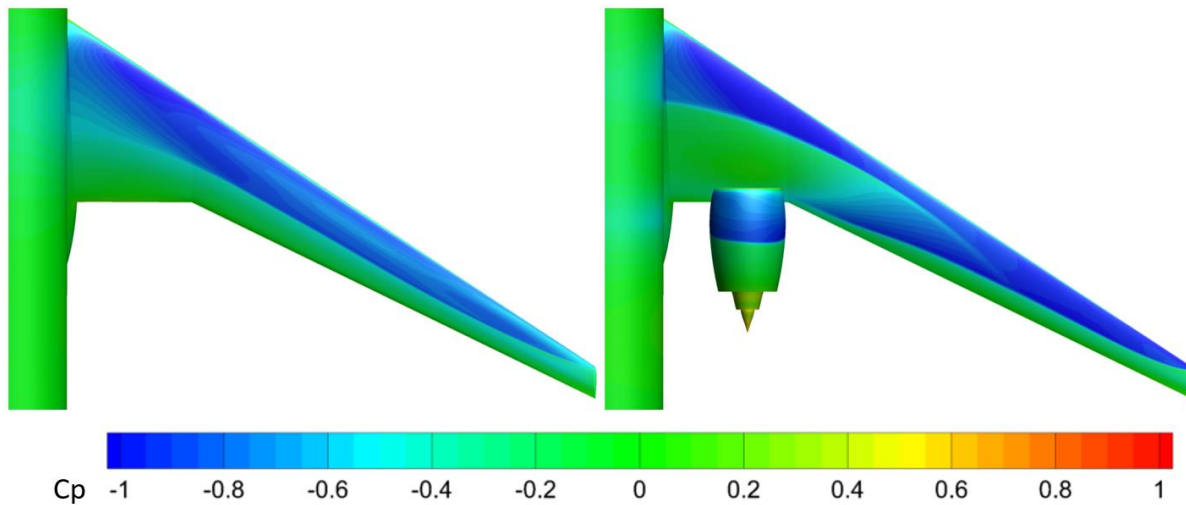


Figure 7 Pressure distribution difference due to engine presence

Furthermore, (see. Figure 7) the shock in the inner wing is amplified and shifted upstream. The total drag increases by 16-50% depending on the position.

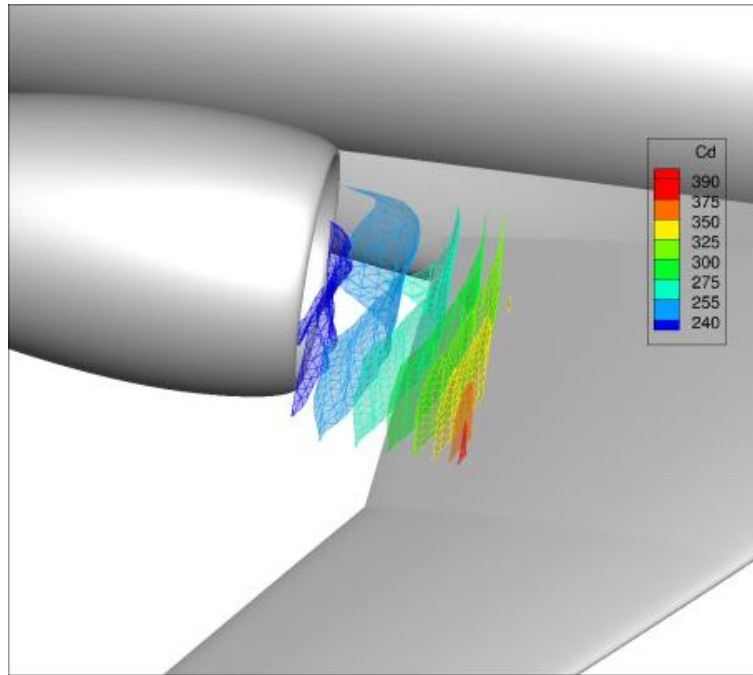


Figure 8 Distribution of total drag

Figure 8 shows a spatial analysis of the total drag surrogate model. The engine is shown in an exemplary position for orientation. The iso-surfaces refer to the envelopes of the engine reference point at the same drag value. A clear correlation between drag and engine position can be seen, which decreases significantly with increasing distance. While the trailing edge sweep angle can be seen in the spanwise position, the vertical component has the least influence on the total drag.

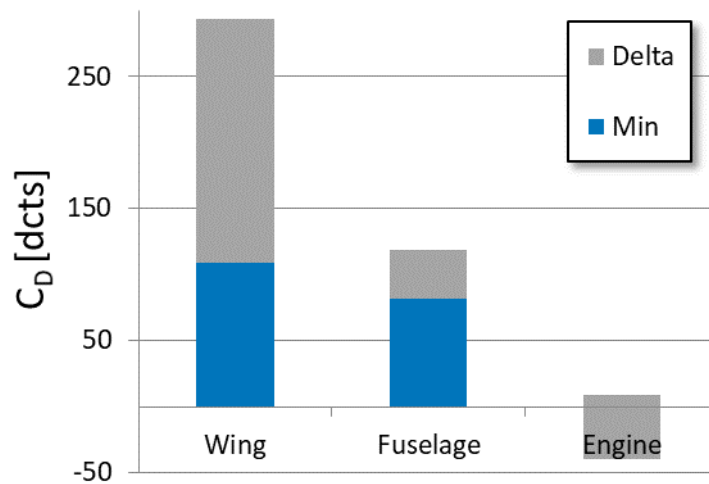


Figure 9 Scope of the component drag values

Figure 9 shows the scope of the drag components in the parameter space. A significantly greater variation of the values can be seen for the wing than for the fuselage. On the engine component, value distribution spreads into negative values. These are caused by a suction peak which forms - as described in literature [3] [16] - due to the interference effect with the upper wing surface. In Figure 10 the partial drags of nacelle and wing are shown spatially. Analogous to Figure 8, an exemplary nacelle is also shown here for spatial classification. The iso-surfaces again represent the envelope of the engine reference point of equal drag values. Two opposite effects can be observed:

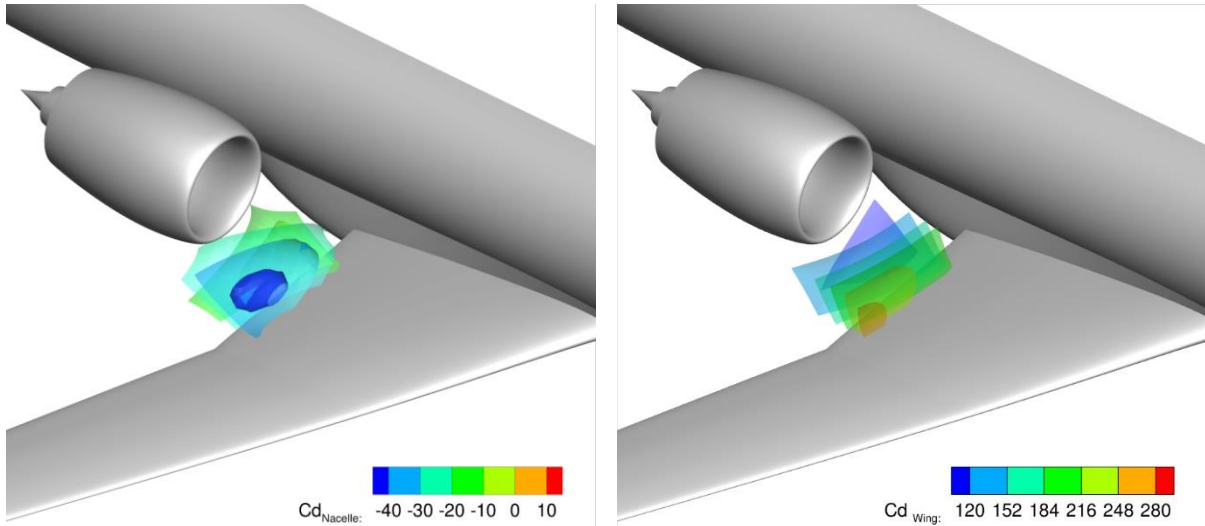


Figure 10 Comparison of wing and engine component drags

On the one hand, there is a spatially delimited area where the minimum of the engine component drag is located, recognizable by the blue bubble above the kink of the wing. On the other hand, this area refers to the largest drag increase on the wing, recognizable by the red iso-surface in this region in the right part of the figure. Both effects thus correspond in a negative way, since the increase in wing drag overcompensates for the positive effects of the engine.

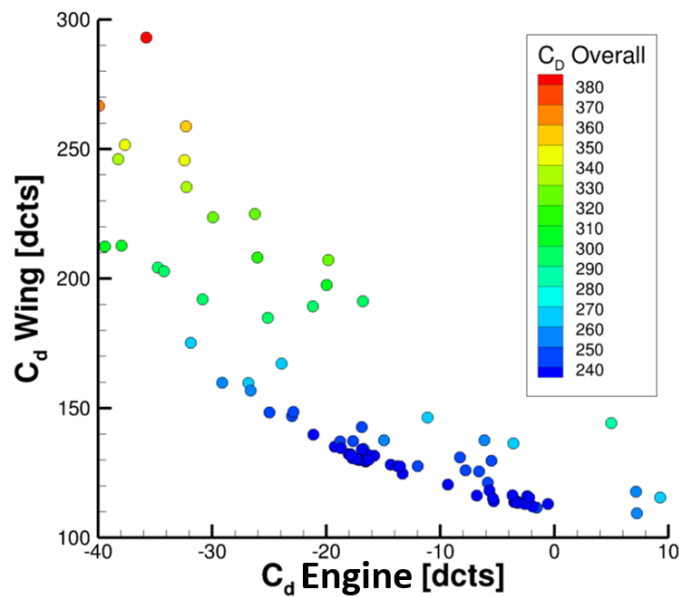


Figure 11 Relation C_d Engine / C_d Wing

Figure 11 shows the results in two dimensions: One can see an increase in wing drag for cases with negative engine drag. The approach to achieve a low-drag overall design is to optimize the geometry of the wing in such a way that on the one hand, the suction peak on the engine is maintained while on the other hand, the negative effects on the wing are minimized.

B. Pylon design

As shown in Figure 11, there is an opposite correlation between engine and wing drag. The position at minimum engine drag thus represents the maximum of the wing drag, which is caused by negative interferences. For the initial modeling of the pylon exactly this position is selected: this assumes that a pylon which can be realized at this position without flow separation also has this property at all other positions.

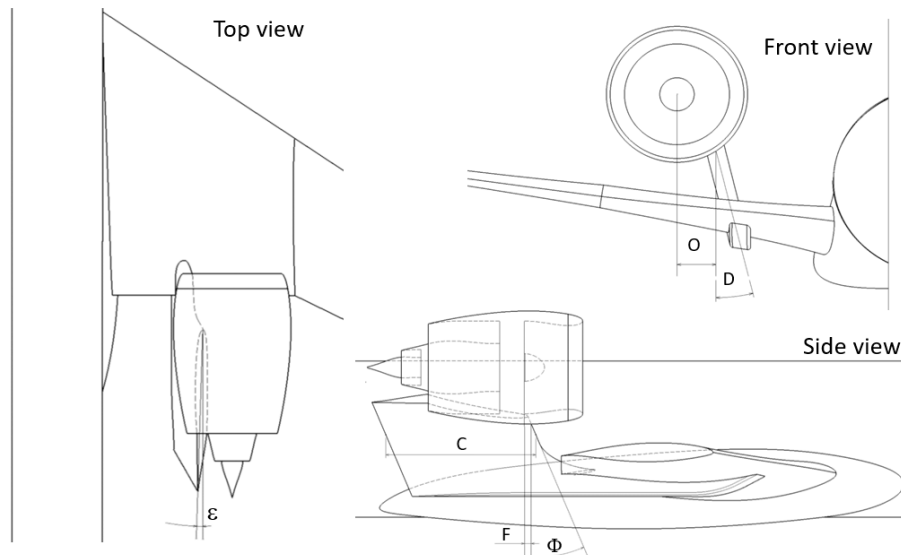


Figure 12 Pylon design parameters

Figure 12 shows the technical boundary conditions: The forces acting on the engine center of gravity apply on the wing box. Since the rear spar does not have the necessary height for this at this point, the pylon is extended vertically downward and thus accesses the main spar via the lower side of the wing. On the engine side, on the annular intersection of a distance F to the fan plane with the engine outer side at distance O and dihedral D , a line with the sweep angle Φ is created, forming the leading edge. At the upper point, a NASA SC(2)0010 wing profile of depth C and twist angle ϵ is placed and extruded along the leading edge towards the wing. At the lower end, an intersection is modeled to the wing root aligned in the direction of flight, and the transition to the wing top is rounded.

The subsequent simulation revealed shock-induced separations, especially in the area of the intersection between pylon and engine. In a manual approach, the parameters of the pylon were modified via an iterative evolutionary process so that the separation regions could be successively reduced and finally avoided.

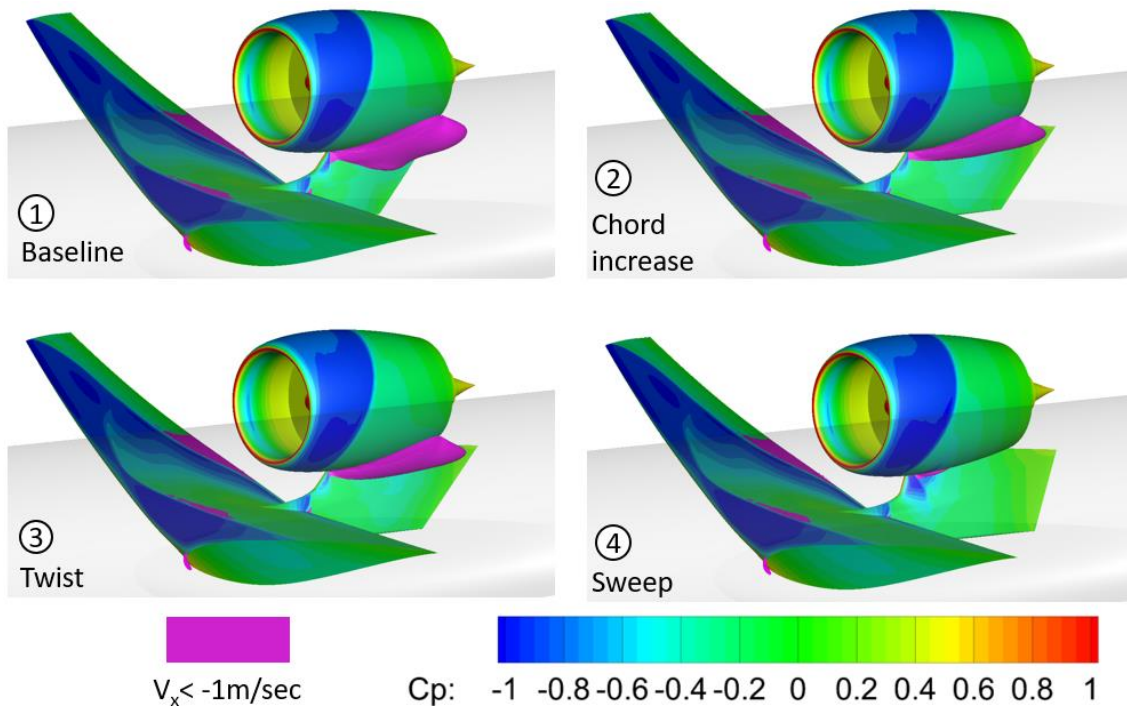


Figure 13 Example pylon design intermediate steps

Figure 13 shows four exemplary intermediate steps of this development. The volumes in which backflow occurs ($v_x < -1\text{m/sec}$) - colored in magenta - indicate the separation regions. By varying the distance O as well as the dihedral, only a shift of the separation regions could be achieved without significant change of the dimensions. Thus, for mechanical simplification, these values were set to zero which thus aligns the pylon parallel to the symmetry plane. The following combinations were found to be key parameters for avoiding the separations:

- Reduction of the pressure gradient by reducing the relative profile thickness via a chord increase (2)
- Introduction of a twist angle of 3° (trailing edge points towards fuselage) (3)
- Changing the sweep angle of the leading edge (4)

For the latter measure, a correlation between the sweep angle and the dimension of the separation region was identified, which showed a clear minimum.

To refine the engine position including the pylon, the positioning simulations were repeated. Since the negative component drag of the nacelle were to be used, and these occurred only in the parameter space with engine/wing overlap, only the 20 positions were considered, which are located in this subspace.

The final selection of the engine position for Concept 3 is less limited than Concept 2, allowing largely free positioning in all three spatial directions. To estimate the location that represents the best position *after* the wing optimization, the experience of Concept 2 wing optimization was used. Figure 14 shows a comparison of the drag components before and after the wing optimization:

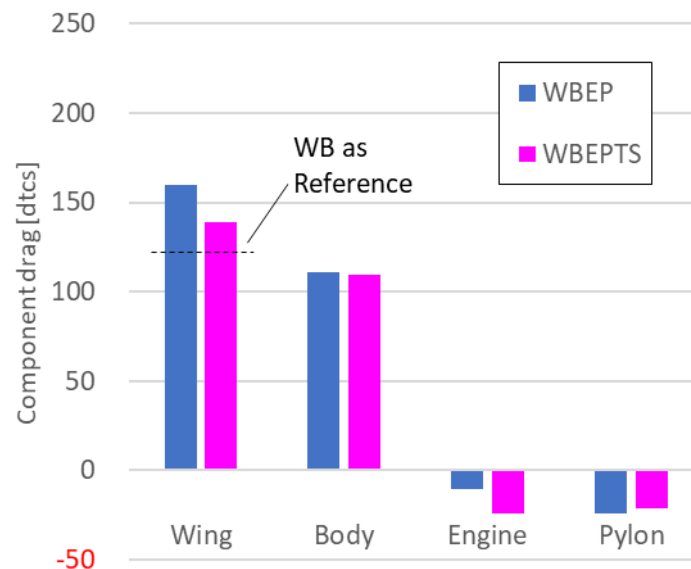


Figure 14 Concept 2 drag components before and after wing optimization

Figure 14 clearly shows which component drags have been changed by the optimization: While only minor differences can be seen in the fuselage and pylon, the component drags of the engine and wing decrease significantly. For the wing component, the value of the wing/body (WB) configuration (see Figure 7) is included for comparison. It is assumed that this value represents the minimum wing drag. Due to the presence of pylon and engine, an additional drag is generated, which is reduced by the optimization. The following therefore applies:

$$C_{D\text{ Wing } WBEPTS} = C_{D\text{ Wing } WB} + I \cdot (C_{D\text{ Wing } WBEP} - C_{D\text{ Wing } WB}) \quad (1)$$

The optimization factor I represents a measure of the achieved Improvement due to the optimization. For Concept 2, a value of $I = 0.492$ could be achieved. In order to estimate the suitable position, the assumed total drag after wing optimization was calculated for different values of I while retaining all remaining component drags for each point of the refined positioning.

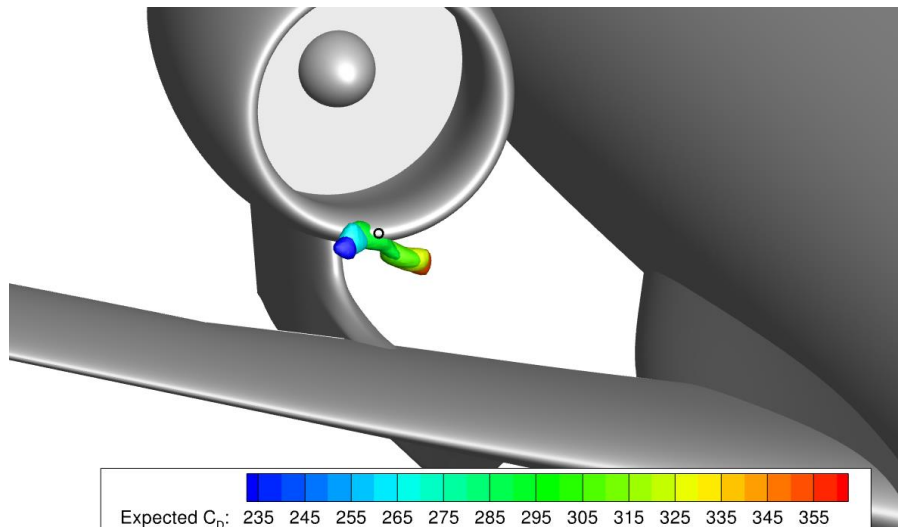


Figure 15 Predicted total drag values after optimization

Based on the results of the Concept 2 optimizations and the assessment of the potentials, an achievable value of 0.3 is assumed for I. The position derived from this value is shown by the circular marking in Figure 15 and is used for the following simulations.

C. Wing optimization

1. Twist optimization

A 5th order Bezier curve is used internally to define the twist distribution. This is shown in blue in Figure 16. The underlying control points are entered as a polygonal curve. As a degree of freedom for optimization, a parameter space of the vertical modification of $+2^\circ/-4^\circ$ was determined for each control point. A DoE with 60 iterations was used to form the surrogate model, followed by an optimization with 20 iterations. The optimization criterion was to minimize the total drag.

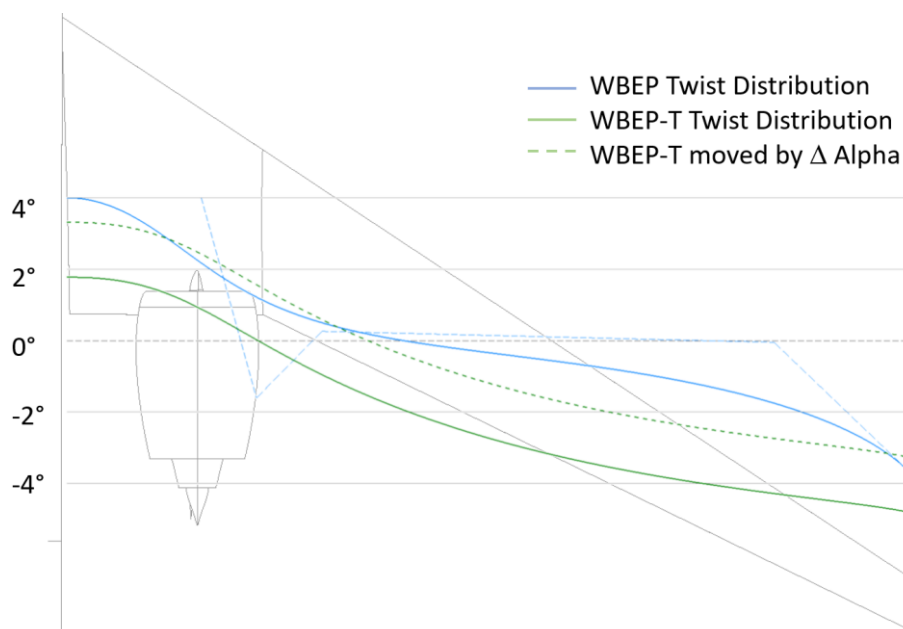


Figure 16 Wing twist distribution curves

Figure 16 shows the twist distribution after optimization in green: It can be seen that - in a first approximation - the complete twist distribution has been shifted towards lower angles thus reducing the incidence angle of the wing. To achieve the boundary condition of $C_L=0.5$, the angle of attack was increased during the simulation. Compared to the initial position, the fuselage and engine thus experience an increased local angle of attack. In the figure, the new twist distribution shifted by the amount of the change in angle of attack is shown in green dashed

lines. The difference between the two curves illustrates a similar local flow condition in the spanwise region of the engine, while in the inner and especially outer regions of the wing the optimization resulted in a significant reduction of the local angle of attack.

2. Shape optimization

To further adapt the wing to the changes introduced by the engine position, the wing airfoils are optimized on several sections in the following.

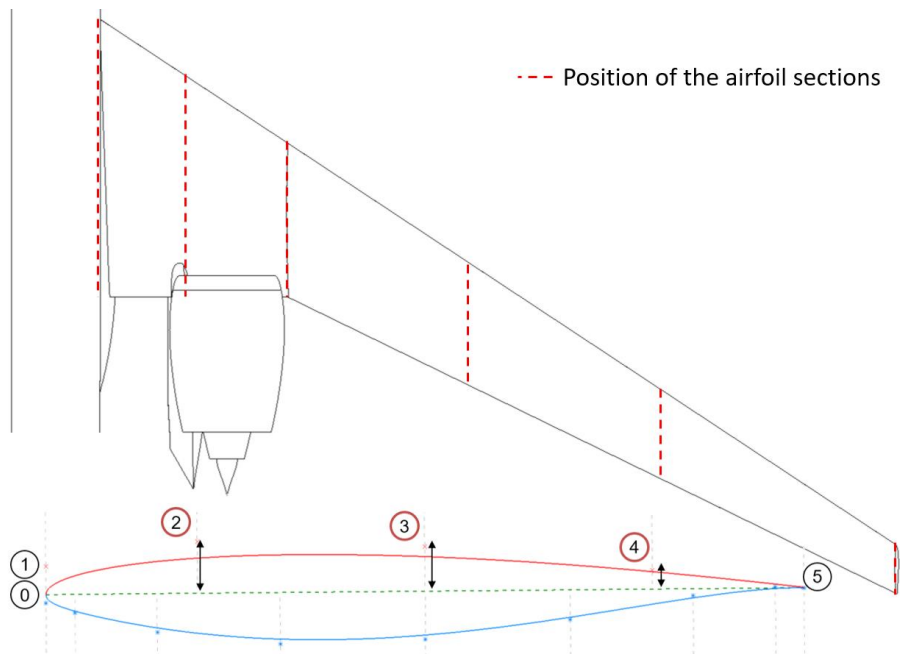


Figure 17 Position and exemplary wing airfoil Bezier curve

The surfaces of the wing are modeled using a total of 6 airfoil sections shown in Figure 17. Assuming that the engine effects have decayed to the wing tip, the profile of the wing tip remains unchanged.

Furthermore, the analysis shows that the presence of the engine and pylon mainly influences the aerodynamics of the upper side of the wing, while the lower side remains almost unaffected. Therefore, the shape optimization focuses only on the upper side of the airfoils.

The airfoils are modeled using 5th order Bezier curves, one is shown as an exemplary airfoil section in Figure 17. The 0th and 1st as well as the 5th control point of each section remain unchanged to ensure a smooth connection to the lower contour and the trailing edge, respectively. As input parameters for the optimization, the vertical positions of the 3 remaining control points are varied. The optimization thus comprises 15 parameters.

After 150 iterations for the definition of the experimental design, 25 iterations were performed for the optimization.

In Figure 18, the normal vectors of the geometric differences of the upper side of the wing before and after shape optimization are overdrawn by a factor of 16:

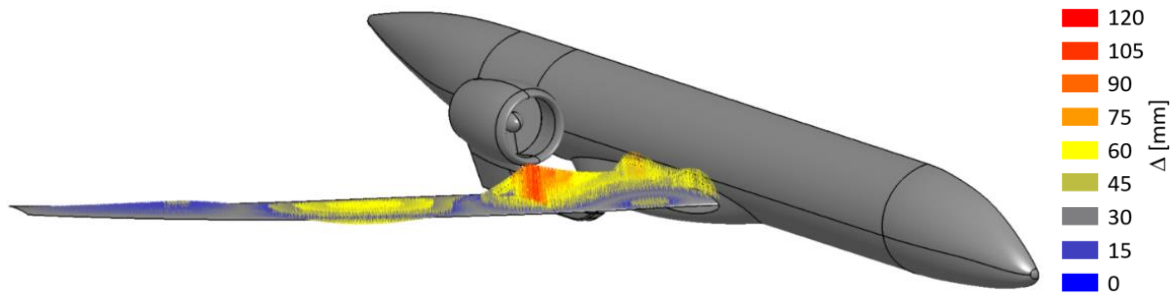


Figure 18 Geometry changes resulting from wing profile optimization

A clear increase in thickness can be seen in the region directly in front of the engine and in the area of the inner wing. In the outer wing area, the resulting wing profile is slightly thinner than the initial position.

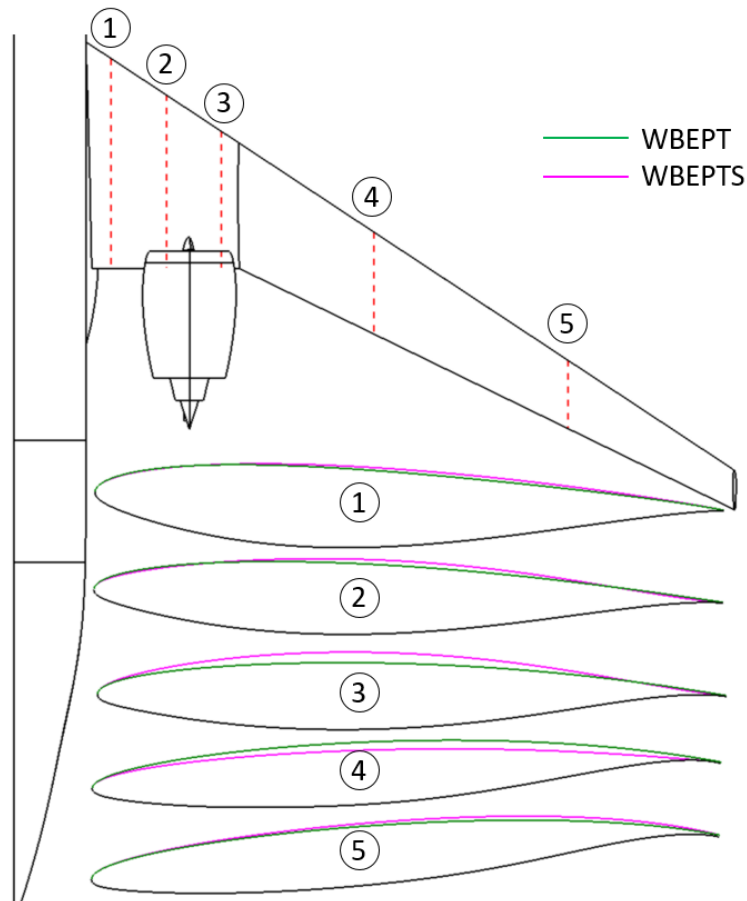


Figure 19 Airfoil changes before and after shape optimization

The profile change is shown in detail in Figure 19. In particular, the thickening in section 3 and the thickness reduction in section 4 can be seen.

V. Aerodynamic analysis

A. Pressure distributions

The surface pressure distributions of the simulation phases are shown in Figure 20. The location of the shock is clearly visible. For the Wing/Body (WB) initial position, the shock position is shown as a magenta curve, and is included in the other views as reference.

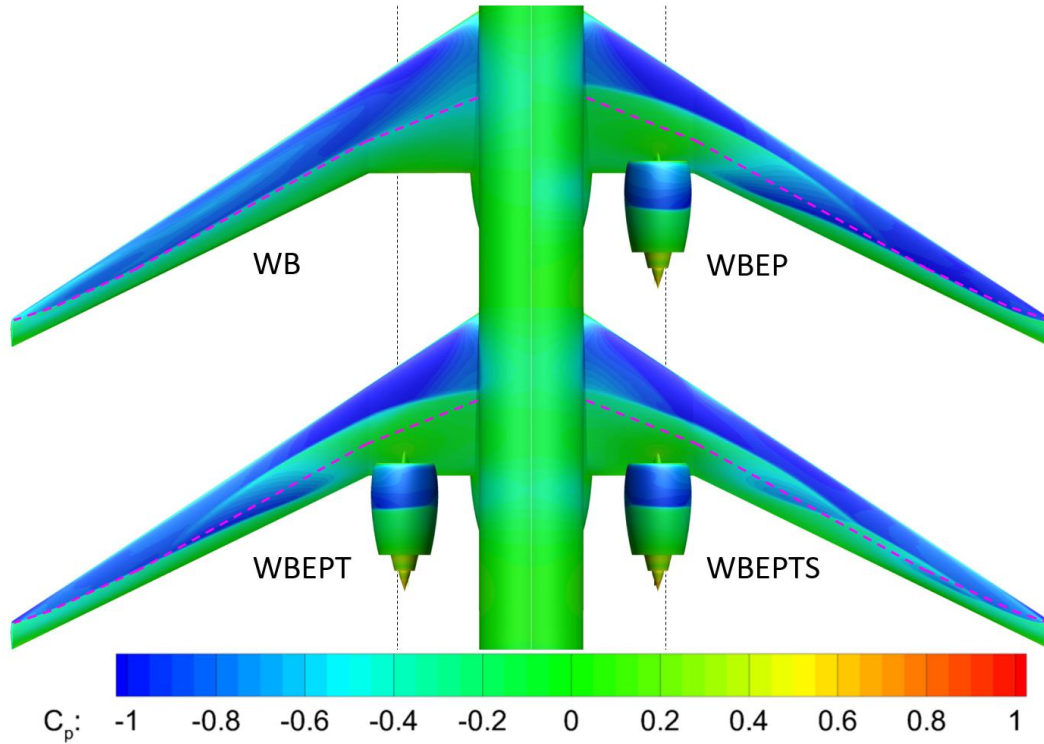


Figure 20 Changes in pressure distribution over the simulation phases

The change in the pressure distributions due to the influence of the engine (transition from WB to WBEP) is clearly visible. As already shown in Figure 7, the shift and intensification of the shock can also be observed here in a comparable manner for the engine with pylon. The changes resulting from the twist optimization (WBEP to WBEPT) are only marginally visible in the pressure distributions. The changes due to airfoil optimization (WBEPT to WBEPTS), on the other hand, can be seen in a reduction of the double shock area in the center outer wing.

Figure 21 shows the pressure distributions in an exemplary airfoil section at $y=25.7\%$ (dotted line in Figure 20).

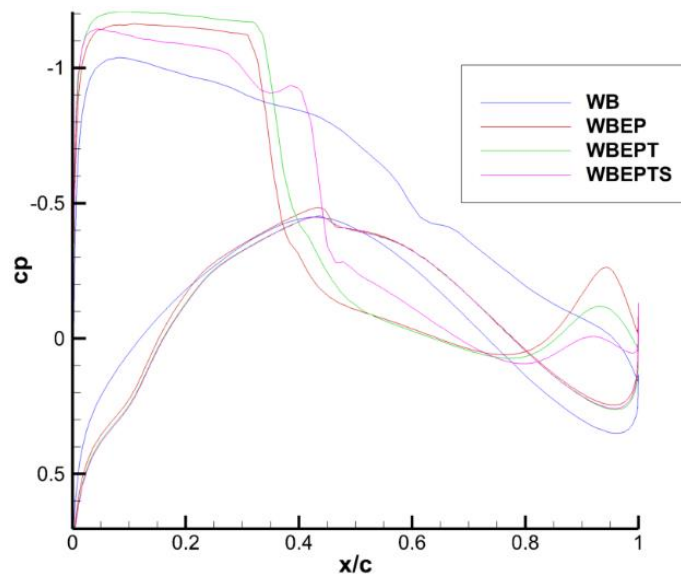


Figure 21 Pressure distribution at the engine section $y=25.7\%$

The change due to the introduction of the engine and pylon, as well as the influence of twist and airfoil optimization, can be clearly seen.

B. Lift distributions

A comparison of the lift distributions over the optimization phases is shown in Figure 21. The lift components of the respective components are color-coded, while the sum of the components represents the local lift. For better classification, the diagrams are supplemented by the elliptical lift distribution and the rear view of the respective configuration for geometric orientation of the engine influence.

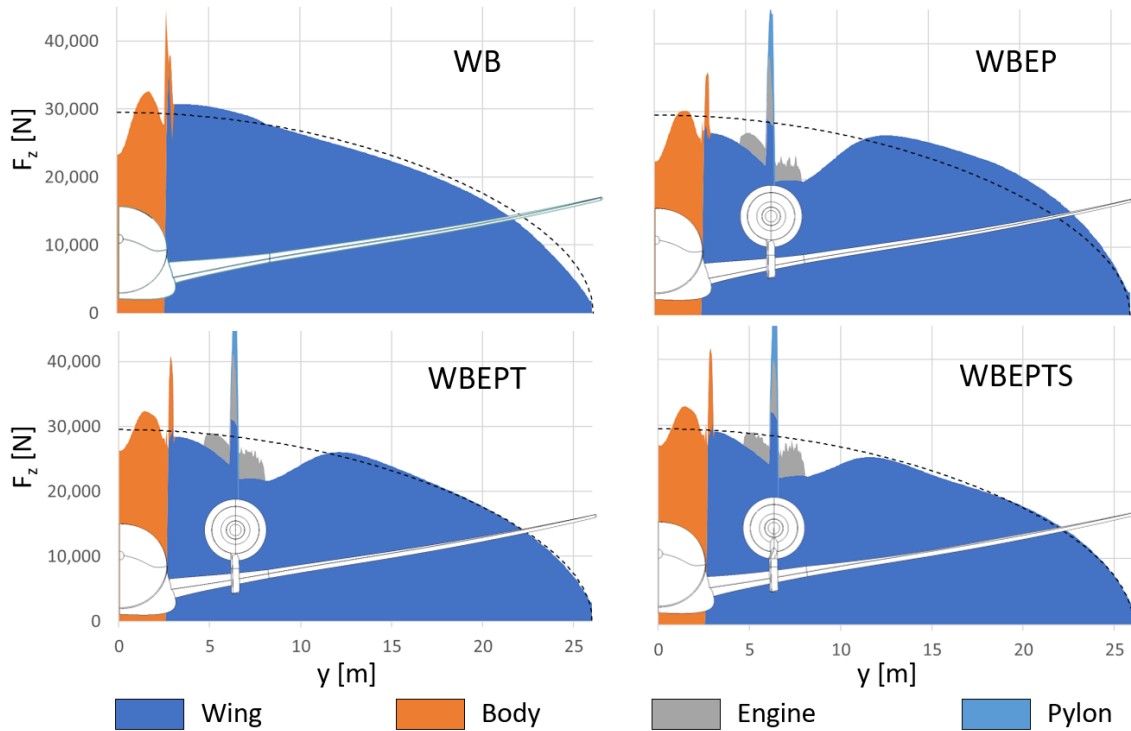


Figure 22 Lift distributions in the simulation course

The wing-body (WB) configuration shows the sub-elliptical lift distribution that was considered in the design to reduce root bending moment. The increase in the angle of attack after integration of the engine and pylon is clearly reflected in the lift distribution in the WBEP configuration: the lift share of the wing shifts significantly outward. This effect could be reduced again by optimizing the twist distribution (WBEPT). Furthermore, the increase in the angle of attack due to this measure can be seen in this plot in the form of the increased lift shares of the fuselage and inner wing. The influence of the airfoil optimization (WBEPTS) on the lift distribution, on the other hand, is less pronounced and relates more to the area around the engine, where a further approximation to the elliptical lift distribution can be observed.

C. Aerodynamic coefficients and interpretation

As described in section IIIA, the component drags were integrated separately for more detailed analysis (see Figure 4). In the following, the progression over the simulation phases is discussed.

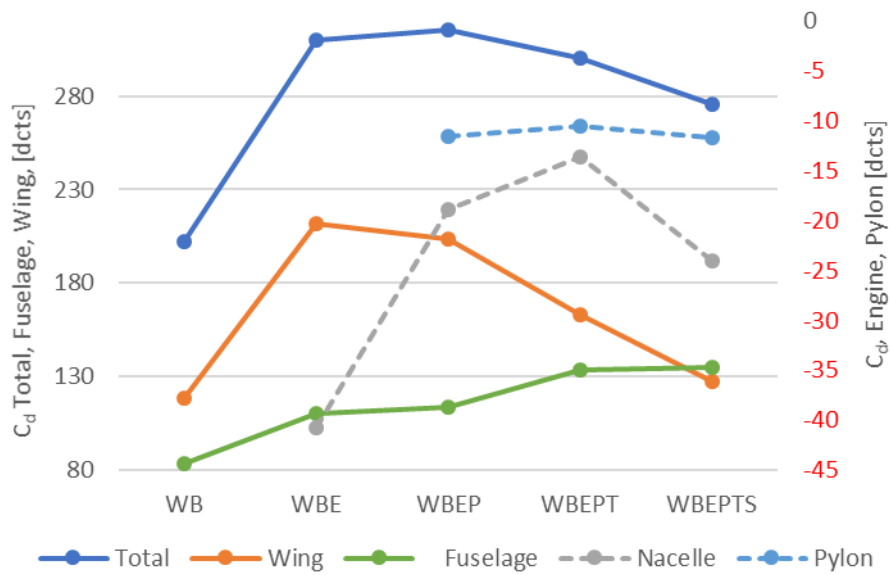


Figure 23 Drag components in the simulation course

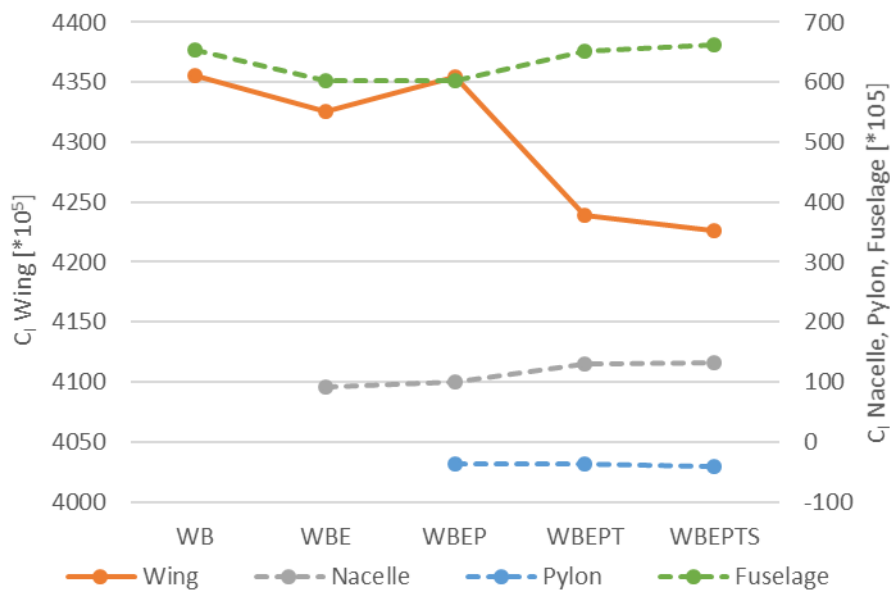


Figure 24 Lift components in the simulation course

Figure 23 and Figure 24 show the drag and lift coefficients of the configuration component wise over the simulation phases.

In the comparison of the simulation phases WB to WBE, the negative drag coefficient of the engine exterior is evident, as are the consequences of its airframe interference in the form of increased drag contributions of the remaining components. In the case of the lift components, the positive contributions from the nacelle are offset by smaller contributions from the wing and fuselage.

The introduction of the pylon in the WBEP simulation phase is most noticeable in the drag components at the engine portion: The beneficial effects were generated at the lower point of the inlet lip. At this location, the pylon is added, and its upstream effect reduces this suction peak. Since the angle of attack remains almost constant at this stage, only small differences in total drag are observed. In the lift coefficients, one can note a negative influence of the pylon, which is compensated by a slight increase in the lift component of the wing.

Optimization of the twist distribution leads to a further increase in the angle of attack, which results in an increase in the lift components of the fuselage and engine - components that do not have to be generated in the wing component, which consequently reduces its contribution. Furthermore (Figure 22), the lift distribution could be approximated to the elliptical distribution. Both effects lead to a reduction of the induced drag, which is reflected in a reduction of the drag component of the wing despite an apparently unchanged pressure distribution. Although the drag components of the engine and fuselage increase, the total drag could be reduced by this measure.

In the final airfoil shape optimization, the boattail angle was increased, especially of the airfoils upstream of the engine (Sections 2 and 3 in Figure 19). This leads to a change in the local angle of attack at the inlet lip, which in turn allows the suction tip to form again. Consequently, the drag of this component is reduced. The likewise improved position of the shock position on the wing further reduces the wing drag, so that in sum the total drag is reduced, although only marginal changes can be observed on the lift side.

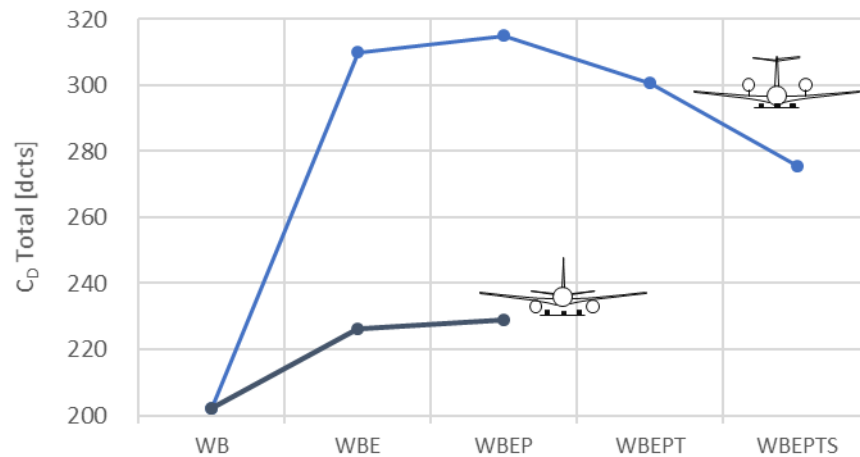


Figure 25 Comparison of the total drag in the simulation course

Figure 25 shows an overview of the total drag of the investigated configuration over the course of the project in comparison with the reference configuration, which was considered in parallel. It becomes apparent that although a significant reduction of the total drag could be achieved by the wing optimizations, no advantage could be gained in comparison to the reference configuration.

VI. Conclusion

In this paper, the aerodynamic design of the configuration with wing-mounted UHBR engines in an over-wing arrangement, which was developed within the AVACON project, was described. The influences of pylon design, as well as wing twist and shape optimization were analyzed and compared with a reference configuration in a classic under-wing engine arrangement.

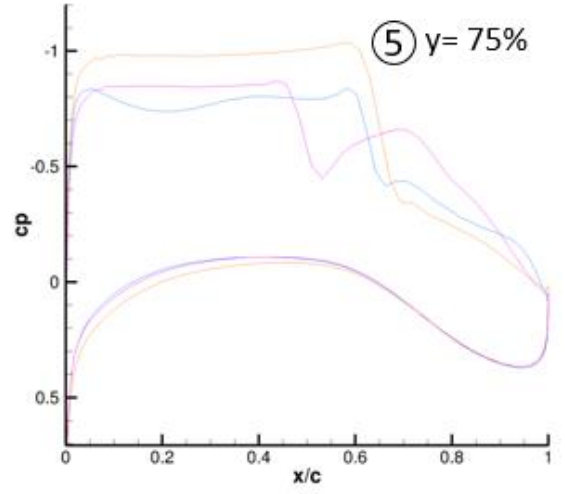
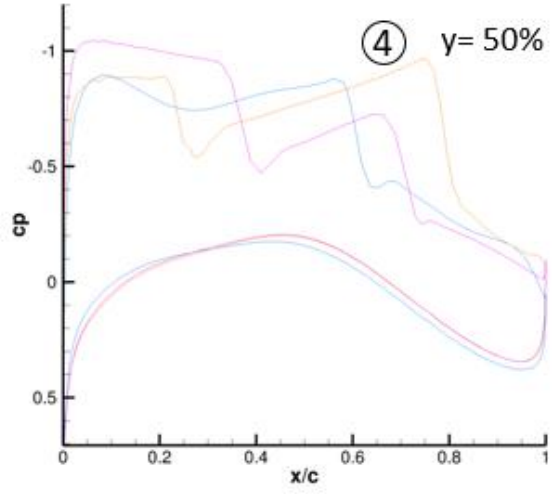
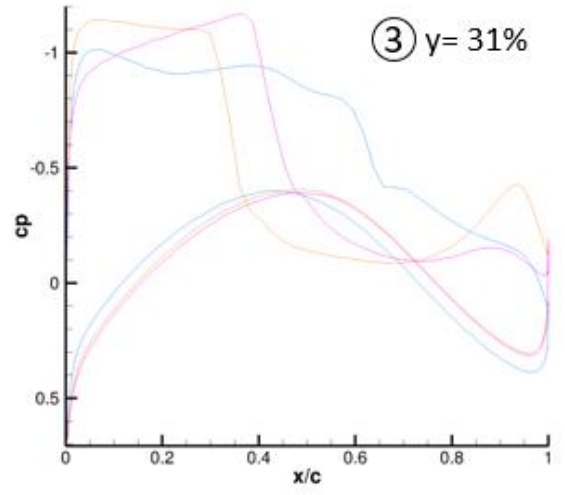
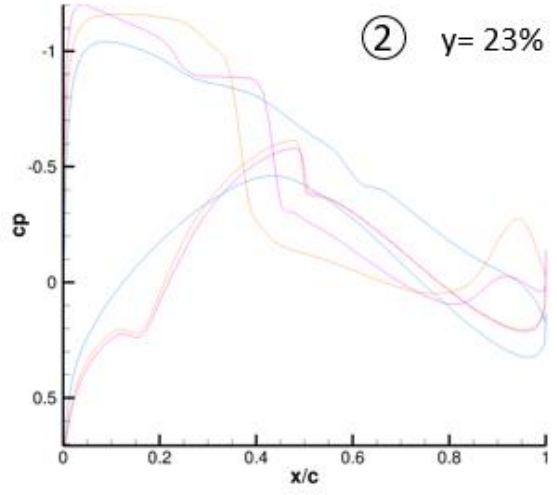
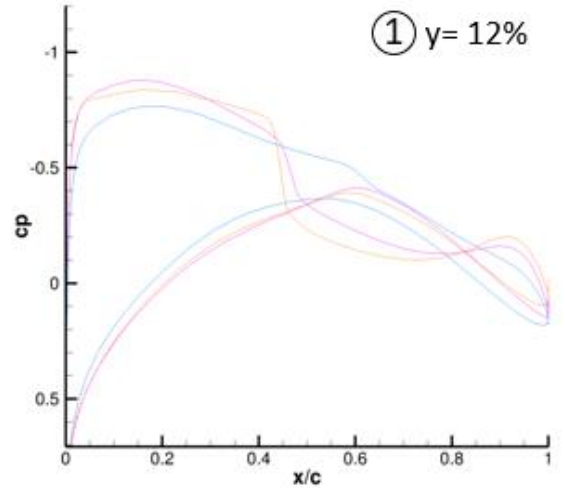
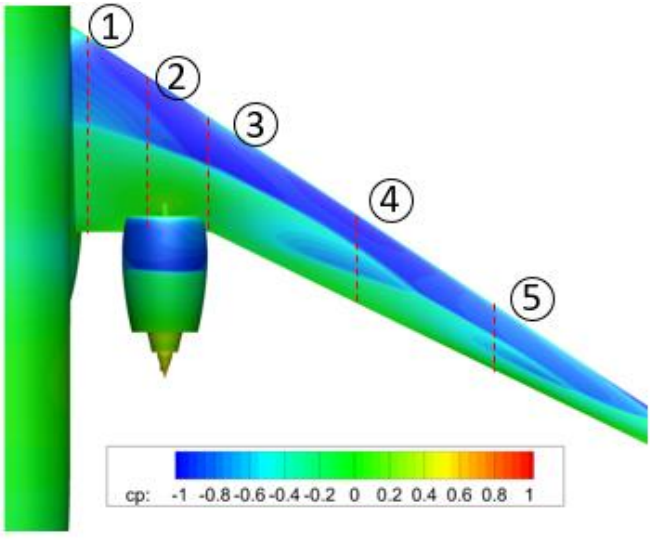
In general, the presence of the engine has an upstream influence on the wing, resulting in a forward shift and amplification of the shock. A suction peak can develop in the gap between the top of the wing and the bottom of the engine, which has a reducing effect on the nacelle drag. The optimization reduced the negative interference with the wing. As a result, the airfoil thickness of the inner wing as well as their boattail angles were increased, which allowed the position of the shock to be shifted back to a certain extent. At the same time, the drag component of the engine was further reduced.

Although the connection to the spar of the wing offers structural advantages, this configuration is the least favorable among the variants studied in the project, since the impact of the pylon reduces the advantageous suction peak at the lower side of the engine.

Appendix

Drag [$C_d * 10^5$]						
Configuration	Alpha	Nacelle	Wing	Fuselage	Pylon	Overall
WB	1.333	118.74	83.58			202.32
WBE	2.910	211.68	109.99	-40.71		309.9
WBEP	2.930	203.71	113.94	-18.88	-11.59	315.07
WBEPT	4.469	163.16	133.38	-13.56	-10.57	300.54
WBEPTS	4.499	127.14	134.64	-24.01	-11.67	275.59

Lift [$C_l * 10^5$]				
Configuration	Wing	Body	Engine	Pylon
WB	4355.72	653.91		
WBE	4325.36	601.40	91.53	
WBEP	4354.91	602.63	100.32	-37.19
WBEPT	4238.96	651.04	130.06	-37.72
WBEPTS	4226.03	661.70	132.35	-41.75



— WB — WBEP — WBEPTS

Figure 26 Pressure Distribution on different airfoil sections

Acknowledgments

We would like to thank the German Federal Ministry for Economic Affairs and Energy for financial support of the AVACON project (grant number 20A1702K). Further thanks go to André Zuchlinski, from Rolls-Royce and Rainer Tegtmeier from AIRBUS for their kind support on structural design considerations and Constance Heykena and Legin Benjamin from TU Braunschweig for deeper insights on nacelle design.

References

- [1] Barche, J. "Tragflügelentwurf am Beispiel des Verkehrsflugzeuges VFW 614." *Zeitschrift für Flugwissenschaften* 22.4 (1974): 101-115.
- [2] Brodersen, O; Taupin, K; Maury, E; Spieweg, R; Lieser, J; Laban, M; Godard, J-L; Vitagliano, P.; Bigot, P., "Aerodynamic Investigations in the European Project ROSAS (Research on Silent Aircraft Concepts)", 35th AIAA Fluid Dynamics Conference and Exhibit , 2005, p.93
doi: 10.2514/6.2005-4891
- [3] Hooker, John R., "Over Wing Nacelle Installations for Improved Energy Efficiency", 31st AIAA Applied Aerodynamics Conference, 2013
doi: 10.2514/6.2013-2920
- [4] Fujino, M., "Design and Development of the HondaJet", *Journal of Aircraft*, 2008, p.755-764
doi: 10.2514/1.12268
- [5] Lange, F., "High fidelity design of the AVACON Research Baseline aircraft based on CPACS data set.", 3AF, 2019
- [6] Wöhler, S.; Hartmann, J., "Preliminary aircraft design for a midrange reference aircraft taking advanced technologies into account as part of the AVACON project for an entry into service in 2028.", DGLR Friedrichshafen, 2019.
doi: 10.25967/480224
- [7] Benjamin, Legin, et al. "Design and Optimization of a Nacelle for a UHBR Turbofan engine using an Intuitive Class Shape Transformation based parameterization."
- [8] Wegener, P., "Integration of fuselage-mounted over-wing engines on a midrange aircraft", ICAS, Shanghai, 2021
- [9] Lange, F; Rudnik, R., "Wing Shape Improvement in the Presence of an Over-the-Wing Mounted UHBR Engine for a Short Range Transport Aircraft" AIAA, 2019
doi: 10.2514/6.2019-2822
- [10] Kirz, J., "Surrogate based optimization of a low boom fuselage wing configuration", AIAA, 2019
doi: 10.2514/6.2018-2849
- [11] Gerhold, T., "MEGAFLOW - Numerical Flow Simulation for Aircraft Design. Overview of the hybrid RADNS code TAU", Heidelberg, Springer Verlag, 2005.
- [12] Spalart, P; Allmaras, S., "A One-Equation Turbulence Model for Aerodynamic Flows", ICCFD7, 1992.
doi: 10.2514/6.1992-439
- [13] Wild, J., "Thrust/Drag Bookkeeping and Aerodynamic Force Breakdown over Components", Braunschweig, DLR-IB-AS-BS-2018-51, 2018
- [14] Wilke, G., "Aerodynamic Optimization of Helicopter Rotor Blades using Variable Fidelity Methods", Braunschweig, DLR, 2017
- [15] Krige, D., "A statistical approach to some mine valuation and allied problems on the Witwatersrand", Witwatersrand, 1951
- [16] Lange, F.; Kotzem, M., "Aerodynamic Interference between Over-Wing-Nacelle and Wing." Deutsche Gesellschaft für Luft- und Raumfahrt - Lilienthal-Oberth e.V.. doi 10.25967/530102.